Original Article

JCBFM

Journal of Cerebral Blood Flow & Metabolism
2017, Vol. 37(4) 1326–1337

DOI: 10.1177/0271678X16654702
journals.sagepub.com/home/jcbfm
SAGE

Impairment of the glymphatic system after diabetes

Quan Jiang[1,2], Li Zhang[1], Guangliang Ding[1], Esmaeil Davoodi-Bojd[1], Qingjiang Li[1], Lian Li[1], Neema Sadry[1], Maiken Nedergaard[3,4], Michael Chopp[1,2] and Zhenggang Zhang[1]

Abstract

The glymphatic system has recently been shown to clear brain extracellular solutes and abnormalities in glymphatic clearance system may contribute to both initiation and progression of neurological diseases. Despite that diabetes is known as a risk factor for vascular diseases, little is known how diabetes affects the glymphatic system. The current study is the first investigation of the effect of diabetes on the glymphatic system and the link between alteration of glymphatic clearance and cognitive impairment in Type-2 diabetes mellitus rats. MRI analysis revealed that clearance of cerebrospinal fluid contrast agent Gd-DTPA from the interstitial space was slowed by a factor of three in the hippocampus of Type-2 diabetes mellitus rats compared to the non-DM rats and confirmed by florescence imaging analysis. Cognitive deficits detected by behavioral tests were highly and inversely correlated to the retention of Gd-DTPA contrast and fluorescent tracer in the hippocampus of Type-2 diabetes mellitus rats. Type-2 diabetes mellitus suppresses clearance of interstitial fluid in the hippocampus and hypothalamus, suggesting that an impairment of the glymphatic system contributes to Type-2 diabetes mellitus-induced cognitive deficits. Whole brain MRI provides a sensitive, non-invasive tool to quantitatively evaluate cerebrospinal fluid and interstitial fluid exchange in Type-2 diabetes mellitus and possibly in other neurological disorders, with potential clinical application.

Keywords

Glymphatic system, magnetic resonance imaging, diabetes, cerebrospinal fluid interstitial fluid exchange, cognitive deficits

Received 17 December 2015; Revised 12 February 2016; 23 April 2016; Accepted 24 April 2016

Introduction

Type 2 diabetes mellitus (T2DM) is a major health problem and is associated with numerous complications including high blood pressure, blindness, non-traumatic lower limb amputations and kidney, peripheral nervous system and cardiovascular diseases and stroke.[1,2] However, despite being an established risk factor for cognitive decline in the elderly population, it is unclear why diabetes contributes to the development and progression of cognitive deficits. The causative roles of DM-associated cerebrovascular dysfunction and neurodegenerative mechanism following abnormal glycemia and insulinemia have been described in the pathogenesis of cognitive impairment.[3–6] However, as the pathological changes in the central nervous system of diabetic individual are usually subtle and multifactorial,[7,8] obtaining imaging biomarkers of DM-associated glymphatic impairment and cognitive decline may permit identification of high-risk patients and the evaluation of potential treatments.

Recent studies[9–13] have fundamentally altered the traditional model of cerebrospinal fluid (CSF) hydrodynamics. Traditionally, it is believed that CSF

---

[1] Departments of Neurology, Henry Ford Health System, Detroit, MI, USA
[2] Department of Physics, Oakland University, Rochester, MI, USA
[3] Center for Translational Neuromedicine, University of Rochester, Rochester, NY, USA
[4] Center for Basic and Translational Neuroscience, University of Copenhagen, Copenhagen, Denmark

Corresponding author:
Quan Jiang, Neurology Department, NMR Laboratory, Henry Ford Hospital, 2799 West Grand Boulevard Detroit, MI 48202, USA.
Email: qjiang1@hfhs.org

produced by the choroid plexus located in all four ventricles flows into the subarachnoid space surrounding the brain and from here exits the cranial cavity by outflow along cranial and spinal nerves, the olfactory bulb, and the arachnoid villi. New imaging measurements have shown that CSF also can be recycled back into the brain and exchanged with interstitial fluid (ISF).[9–14] The dynamic exchange of CSF with ISF is identified as the glymphatic system. The glymphatic system provides a pathway of highly organized convective fluid flow that drives clearance of interstitial solute from the brain parenchyma. The glymphatic system is primarily active during natural sleep and impairment of the glymphatic clearance is involved in the development of neurodegenerative conditions, including Alzheimer's disease and traumatic brain injury (TBI),[9,11,13] which are often linked to sleep disorders. However, it is not known whether diabetes impairs the glymphatic activity. Since diabetes is linked to vascular pathology and increases the risk of developing small vessel disease with enlargement of the perivascular space,[15,16] it is of particular interest to establish whether diabetes impairs glymphatic activity. Also, diabetes is associated with reduced performance on cognitive function.[17–19] Chronic hyperglycemia and microvascular disease contribute to cognitive dysfunction in both type 1 and 2 diabetes, and both disorders are associated with decrements of attention and executive functioning as well as mental and motor slowing.[17–19] However, the exact mechanisms by which diabetes trigger cognitive dysfunction are not well understood.[17,18] In this study, we employ MRI to dynamically image contrast agents in CSF as well as 3D confocal microscopy of the brain-wide distribution of fluorescent tracers to evaluate, for the first time, the temporal and spatial profiles of paravascular CSF-ISF exchange throughout the brain and related functional deficits and impairment of the glymphatic system after T2DM.

Materials and methods

All experimental procedures were conducted and performed in accordance with guidelines of National Institute of Health (NIH) for animal research under a protocol approved by the Institutional Animal Care and Use Committee of Henry Ford Hospital, and experimental guidelines of ARRIVE (items 8, 10 to 13). All experimental procedures were approved by the Institutional Animal Care Committee of Henry Ford Hospital.

Animal model and groups

Male Wistar rats, 13 months of age ($n = 33$) were subjected to intraperitoneal (IP) injection of 210 mg/kg of nicotinamide (NTM) and streptozotocin (STZ, 60 mg/kg), which has been demonstrated to produce noninsulin-dependent DM syndromes that resemble human type 2 diabetes.[20,21] This animal model mimics some pathological manifestations of human T2DM, including increase in blood glucose, insulin secretory dysfunction, and glucose intolerance, but not hyperinsulinemia and obesity.[20,22,23] The diabetic state was assessed two days after STZ injection and weekly thereafter by measurements of non-fasting plasma glucose concentration. These rats develop hyperglycemia at two weeks and became DM (non-fasting plasma glucose concentrations >250 mg/dL) two months after STZ-NTM administration, which resembles the clinical manifestation of T2DM.[24] Four rats failed to develop hyperglycemia and three DM rats died within one month after NTM and STZ injection (9% mortality rate). These animals were excluded from further experiments.

A total of 44 rats were assigned into non-DM ($n = 18$) and DM ($n = 26$) groups. MRI measurements were performed in five non-DM and five DM rats. Ex-vivo fluorescence imaging was performed on DM and non DM rats ($n = 17$/group). DM and non-DM rats were enrolled in the Morris water maze test (MWM, $n = 10$/group). However, 40% of DM rats (4 of 10) subjected to the MWM were excluded from the cohort based on their skin condition (two rats developed skin ulcers) and poor performance during the initial MWM trials (two rats were unable to keep their heads above water/drowning after the first two trials). The odor recognition test was performed on six DM and six non-DM rats. However, 33% of rats (two DM and two non-DM) failed to explore or approach any beads during the novel-odor habituation phase and were excluded from the odor recognition test.

MRI measurements

MRI measurements were obtained using a 7T scanner with a birdcage type coil as the transmitter and a quardrature half-volume coil as the receiver. During MRI measurements, anesthesia was maintained using medical air (1.0 L/min) with isoflurane (1.0–1.5%). Stereotactic ear bars were used to minimize movement, and rectal temperature was maintained at $37 \pm 1.0^{\circ}$C using a feedback controlled water bath.

At each MRI session, a fast gradient echo imaging sequence was used for positioning of the animal in the magnet, and a spin echo sequence of T_2-weighted imaging (T2WI) was acquired for detection of brain tissue changes in the DM rat. The T2WI contained six sets of images using echo time of 15, 30, 45, 60, 75, and 90 ms; repetition time of 4.5 s, and $32 \times 32\,\text{mm}^2$ field-of-view (FOV), 128×128 matrix, 1 mm slice thickness of 13 slices.

The dynamic CSF-ISF exchange was measured using 3D T1-weighted MR images (T1WIs) with Gd-DTPA contrast agent followed with a contrast enhanced MRI (CE-MRI) protocol.[14] 3D T1WIs were obtained with echo time of 4 ms, repetition time of 15 ms, flip angle of 15°, $32 \times 32 \times 16\,\text{mm}^3$ field-of-view (FOV), and $256 \times 192 \times 96$ matrix interpolated to $256 \times 256 \times 64$ voxels ($0.125 \times 0.125 \times 0.125$ mm) for analysis. Dynamic 3D T1WIs were acquired continuously for 6 h with three baseline scans followed by intra-cisterna magna (ICM) Gd-DTPA contrast (21 mM, Gd-DTPA, MW 1 kD) delivery via the indwelling catheter while MRI acquisitions continued.[14] A total of 80 µl of the paramagnetic contrast agent was delivered intrathecally at an infusion rate of 1.6 µl per minute (total infusion time = 50 min).

Ex-vivo fluorescence imaging

A mixture of 0.1% fluorescein isothiocyanate (FITC)-conjugated dextran 500 (FITC-d500, MW 500 kDa) and Texas Red-conjugated dextran 3 (TR-d3, MW 3 kDa) dissolved in artificial CSF was injected into ICM. TR-d3 was selected to roughly correspond with the molecular weights of Gd-DTPA (MW ~ 1 kDa) and FITC-d500 was employed for evaluating the clearance of large size molecular; 30, 180, and 360 min after injection, animals were transcardially perfused with heparinized saline and 4% paraformaldehyde, and the brains were removed and post-fixed overnight at 4°C. Six coronal vibratome sections (100 µm/section) spaced as 300 µm intervals at the level of dorsal hippocampus (bregma −2 to −4) were mounted with VECTASHIELD Mounting Medium (Vector Lab). Tracer distribution was imaged under a fluorescence microscopy using micro computer imaging device (MCID) analysis system (Imaging Research Inc.). For quantification, the distribution of TR-d3 was imaged with the corresponding red emission channel within the hippocampus and hypothalamus. The fluorescence intensity within each ROI was calculated using the corresponding non-injected control slices as background level with the MCID. Data are presented as the % of TR-d3 exposed area within the hippocampus and hypothalamus.

Functional outcome

All functional outcome tests were performed by observers blinded to the group allocation. For assessment of cognitive impairments, the spatial learning function was measured with MWM test performed daily for five days before sacrifice.[25,26] Briefly, the experimental apparatus consists of a circular water tank (140 cm in diameter) which is placed in a large test room with many external cues (e.g., pictures, lamps, etc.) that are visible to the rats. A transparent platform (15 cm in diameter) is submerged 1.5 cm below the surface of the water at a random location within the Northeast quadrant of the maze. For each trial, the rat was placed randomly at one of four fixed starting points (north, south, east, and west), and allowed to swim for a maximum of 90 s. The latency to find the hidden platform and the time spent within the correct quadrant are recorded. Data are presented as the percentage of time spent within the correct quadrant relative to the total amount of time spent to find the platform.

The olfactory learning and memory were measured with an odor recognition test before sacrifice.[27] Briefly, identical round wooden beads (Woodworks Ltd.) were placed in the cages of two individually housed donor rats for one week without bedding change to acquire animal specific odors (designated as N1 and N2). During the initial familiarization period (two days before testing), four unscented wooden beads (designated as F1–F4) were introduced into the home cage, where the testing rat would be familiarized the presence of the beads for 24 h. On the following day (one day before testing), the four now-familiar beads (F1–F4) were removed for 1 h. After this 1-h period, three familiar beads (F1–F3) and a novel-odor scented wooden bead (N1) were randomly placed into the home cage for three 1-min trials with 1-min inter-trial intervals. The timing of the 1-min trial is initiated when rat begins approaching any bead. This procedure produces habituation to N1 while minimizing olfactory adaptation. Exploration time for each of the four beads was recorded by experimenters blinded to which beads were familiar or novel (beads were number-coded). The odor recognition memory test was performed 24 h after the novel-odor habituation phase. Four beads including two familiarized home cage beads F1 and F2, a recently familiarized bead N1, and a novel-odor bead N2 were placed in the home cage, following the same procedure outlined for the habituation phase. Exploration time for each beads was recorded. The focus of the test was to assess the nonspatial social odor-based novelty recognition for N2 bead and the overnight memory for the N1 bead. Good odor recognition memory was indicated by more time spent exploring N2 than N1 and other beads in the trial. Data are presented as the percentage of time spent on N2 relative to the total amount of time spent with all beads.

Data analysis

Data analysis was performed in a blind fashion. The general MRI processing procedure consisted of brain extraction, registration to correct head motion, and voxel-by-voxel conversion to percentage of baseline signal using SPM8 (http://www.fil.ion.ucl.ac.uk/spm/). Generally, the T1 images in this work include all the head tissues. Therefore, the first necessary step is to remove non-brain tissues in order to reduce the computations and improve the performance of following registration steps. To do this, for each case, first we draw manually a mask on the standard deviation (STD) map (computed from STD of time courses) on each coronal section, one by one, in order to encompass all the brain. Second, scan-to-scan misregistration caused by head movement was corrected by rigid-body alignment of each scan to the time-averaged (mean) image. Third, to ensure that voxel intensity represents percentage change relative to the average baseline images, all time series images were subtracted and divided by the baseline average image. The signal changes measured on the T1-weighted MRIs over time in preselected anatomical areas were used to obtain the average time evolution curve (TEC) of regional tissue uptake of the paramagnetic contrast agents. The T1-weighted averaged baseline images as well as the contrast-enhanced T1-weighted MRIs were used to anatomically guide placement of the ROIs. From the TEC, residual intensity (signal intensity at end of experiment minus baseline intensity) was calculated for comparison between DM and non-DM rats. We also fit the TECs to a simple two-phase model based on exponential curves[28] to derive clearance time constant. The first phase models the accumulation of the CA in each voxel during the injection period. This phase was not investigated in this manuscript. However, the second phase which models clearance of the CA from each voxel is modeled by an exponential decay, $I(t) = I_{\max} (e^{-(t-tm)/\tau 2})$ for $t > t_m$, in which $I_{\max}$ is the maximum intensity accrued at t_m. τ_2 is the clearance time constant and is estimated from the data. Clearance rate constant ($1/\tau_2$) is used in current study and the larger this value is, the faster the CA clearance from the tissue.

Cluster analysis

Nonparametric segmentation to group voxels in the MRI images on the basis of similar kinetics was performed using a k-means cluster algorithm from each of the 4D T1-weighted MRIs, as in previous investigation.[14] A volume-of-interest mask containing the brain only was created for the cluster analysis. The number of clusters (*K*) used was determined by the *K* that was able to segment out voxels adjacent to the large vessels, such as basilar artery (including pituitary recess) and olfactory artery complex. This was done on an interactive, per animal basis. The number of clusters that provided the most ideal visualization of paravascular inflow conduits was five clusters. The five clusters were examined visually and coregistered with the corresponding contrast-enhanced and anatomical MRIs to verify the positions of the clusters in relation to the large vessels. The number of voxels and TECs for each cluster was extracted for further processing.

Statistics

Observations are presented as mean ± standard errors. Correlations between behavioral data and the MRI or fluorescence imaging measurements were analyzed by Pearson correlation coefficients. To test the effect of DM on MRI and ex-vivo fluorescent tracer distribution and MRI clearance rate constant, a two-sample *t*-test was performed, with $p < 0.05$ described as significantly different.

Results

Visualizing CSF-ISF exchange in the live rat brain with and without DM

We first evaluate whether glymphatic CSF-ISF influx and efflux functions are impaired after diabetes. As demonstrated in Figure 1, the 3D dynamic T1WIs exhibit influx of MRI contrast agent, Gd-DTPA, over the 6-h infusion period in DM and non-DM rats. In non-DM rats, the dynamic time series of T1WIs clearly revealed the time-dependent anatomical routes of paravascular influx and anatomic enhancement, including: (i) arrival of paramagnetic contrast agent in the cisterna magna (C, 0), (ii) appearance of contrast in the pituitary recess 15 min after injection (C, 15 min), (iii) continued transport along the olfactory arterial complex and into the olfactory bulb 30 min after injection (C, 30 min), (iv) contrast enhancement in brain 90 min after Gd-DTPA injection (C, 90 min), (v) contrast enhancement in brain during the middle of the experiments (C, 3 h), (vi) contrast enhancement in brain at the end of the experiments (6 hours after initial Gd-DTPA injection, C, 6 h). Figure 1(f) to (g) is the corresponding parallel ex-vivo confocal imaging after ICM injection of FITC-d500 (MW 500 kD, green) and TR-d3 (MW 3 kD, red) molecular tracers. MRI and fluorescent images demonstrate the evolution of tracer distributions, confined in paravascular arteries within 30 min, low TR-d3 molecular tracer or Gd-DTPA led to rapidly CSF influx through the para-arterial space of penetrating arteries located on the surface of brain at 30 min (C, F), TR-d3 or Gd-DTPA signals occupied most brain areas and more deep brain penetration of FITC-d500 along the paravascular space 3 h after injection (C, F), although FITC-d500 signal still confined within para-arterial space, most TR-d3 was cleared from the brain (F) and hippocampus (G) 6 h after the injection.

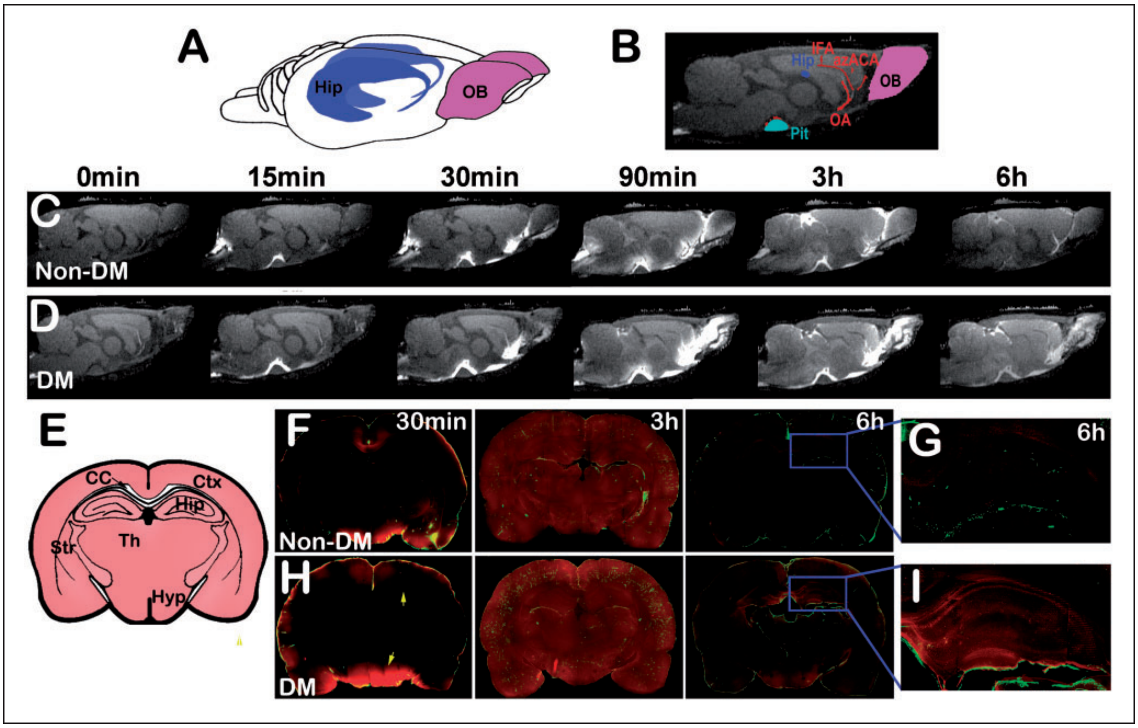

Figure 1. DM-induced dynamic tracer concentration changes: 3D (a) and 2D T1WI (b) visualization of key anatomical structures in the rat brain, the pituitary (Pit, light blue), hippocampus (Hip, dark blue), the olfactory bulb (OB, purple), and relevant arterial segments (red) including the olfactory artery (OA), azygos of the anterior cerebral artery (azACA), and the middle internal frontal artery (IFA). The time series of MRI images (c, d) demonstrates early influx (0–30 min) and anatomic enhancement 90 min, 3 h and 6 h after ICM injection of Gd-DTPA in non-DM (c) and DM (d) animals. Panel E is the schematic representation of coronal sections at the level of bregma −3.0 mm showing key anatomical structures including cortex (Ctx), hippocampus (Hip), corpus callosum (CC), striatum (Str), thalamus (Th), and hypothalamus (Hyp). The corresponding fluorescence microscopic images of coronal brain sections after ICM injection of TR-d3 (red) from the same non-DM (f, g) and DM rats (h, i) show that 30 min after tracers injection, TR-d3 was accumulated mainly on the surface of the brain in both non-DM (f) and DM (h) rats. By 3 h after the ICM injection, TR-d3 occupied most brain areas in both non-DM and DM rats. While TR-d3 signal measured 6 h after injection was essentially undetectable in the non-DM brain including the hippocampus area (g), persistent accumulation of TR-d3 in the hippocampus and hypothalamus (arrows in h) was detected in T2DM rats 6 h after the injection (i).

Compared with the non-DM rat (C, F, G), the time point matched DM rat (D, H, I) exhibits several different features in the tracer distribution, i.e.: (i) more enhanced areas involved during the initial paravascular arterial influx (D vs. C, 15–90 min); (ii) areas with increased signal intensity (tracer concentration) are more confined close to paravascular arteries than in the deep brain tissues; (iii) the overall intensity (tracer concentration) during the middle of the experiment (3 h, D vs. C) is higher; (iv) the residual intensity (or tracer concentration) 6 h (D vs. C) after Gd-DTPA injection is also higher. Consistently, the fluorescent imaging data confirmed MRI findings, that more tracer accumulation is present in the areas close to paravascular arteries during the middle of the experiment (3 h, H vs. F) and also increased tracer concentration was present at end (6 h, H vs. F) of the experiment in the DM compared with non-DM animals. Also, in the DM rats, a persistent retention of TR-d3 in the hippocampus region was detected in the DM brain (I) 6 h after tracer injection compared with the non-DM (G) rats.

Although para-arterial inflow of tracer is clearly demonstrated in this study in Figure 1, para-venous outflow is another important component of the glymphatic pathway. Previous studies have demonstrated that para-venous structures are major outflow routes for interstitial hTau[29] and OA-647.[11] To image para-veins outflow, we performed T1WIs on a major vein, the superior sagittal (SS) sinus, to demonstrate tracer efflux along the SS sinus. Figure 2 shows horizontal sections of T1WIsfrom a non-DM rat head at the level of the SS sinus before injection (A) and 180 min after (B) finishing infusion of Gd-DTPA into the subarachnoid cisterna magna. The SS sinus appears as a dark line in the middle of the two hemispheres (arrow,

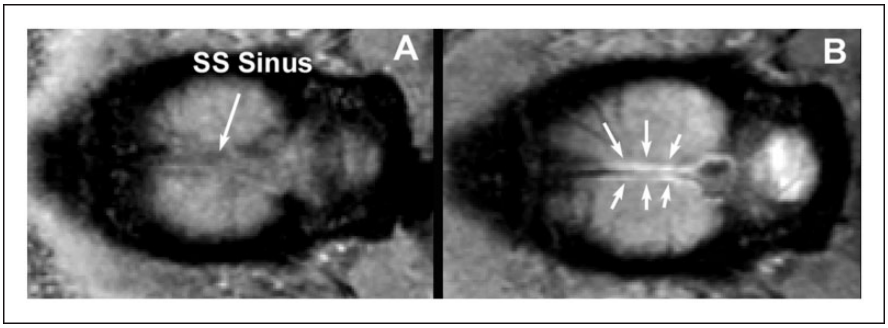

Figure 2. Horizontal sections of T1-weighted MRI images from a rat head at the level of the SS sinus before (a) and 180 min after (b) finishing infusion of Gd-DTPA into the subarachnoid cisterna magna.

A) before injection and, after infusion of contrast; symmetric areas adjacent to the SS sinus appear bright (arrows, B), which is comparable to the previous study.[30]

Quantitative characterization of CSF-ISF exchange in the live rat brain with and without DM

To compare the relative kinetics within the subregions in the brain, TECs were calculated after injection of Gd-DTPA in the hippocampus (Figure 3(a)) and hypothalamus (Figure 3(c)). Within the hippocampus ROI (Figure 3(a)), the time courses of signal intensity changes induced by Gd-DTPA concentration were similar between DM and non-DM animals during the early period to reach peak concentration plateau ($\sim$150–250 min, Figure 3(a)). However, the DM rats exhibited higher residual intensity (signal intensity at the end of experiment minus baseline intensity) compared with the non-DM rat. The DM rats exhibited significantly increased residual intensity ($p = 0.005$, 772% of control) in the hippocampus compared with the non-DM rat. We also fitted the TECs to a simple two phase model based on exponential curves.[28] The Gd-DTPA clearance rate constant, $1/\tau_2$, was 3.4 times slower ($p = 0.022$) in DM ($1.35 \times 10^{-3}\,\text{min}^{-1}$) than non-DM ($4.61 \times 10^{-3}\,\text{min}^{-1}$) rats.

The TECs exhibited regional differences between non-DM and DM animals. The hypothalamus (Figure 3(c)) and olfactory bulb (OB, Figure 3(e)) recess in DM rats exhibited smaller differences in Gd-DTPA residual intensity (hypothalamus, $p = 0.012$, 333% of control; OB, $p = 0.015$, 235% of control) and clearance rate constant (hypothalamus, $p = 0.040$, 2.73 times slower, 2.46 vs. $6.71 \times 10^{-3}\,\text{min}^{-1}$; OB, $p = 0.151$, 1.98 times slower, 2.44 vs. $4.83 \times 10^{-3}\,\text{min}^{-1}$) than non-DM animals. The overall effects of DM versus non-DM reflect higher residual concentrations at 6 h and slower clearance rate constants which are caused by reduced clearance of Gd-DTPA during CSF-ISF exchange.

Quantitative measurement of fluorescent CSF-ISF tracer distribution

To further examine the glymphatic system function in the DM brain, the distribution of fluorescent tracers TR-d3 and FITC-d500 was measured 0.5, 3, and 6 h after ICM injection. While the high MW tracer-FITC-d500 was confined within the paravascular compartment throughout the experiment, brain wide accumulation of the low MW tracer-TR-d3 was detected 3 h after ICM injection with comparable fluorescent levels in the hippocampus and hypothalamus of DM and non-DM rats. However, TR-d3 fluorescent signals are essentially undetectable in the non-DM brain including the hippocampus and hypothalamus regions by 6 h after injection. DM rats exhibited significantly higher TR-d3 fluorescent levels in the hippocampus (Figure 3(b)) and hypothalamus (Figure 3(d)) than the non-DM rats 6 h after tracer injection. These data are consistent with the MRI findings on the retention of Gd-DTPA in the DM brain via slow ISF-CSF clearance.

Cluster analysis of CSF-ISF exchange in the live rat brain with and without DM

We also performed a cluster analysis on a series of four midline sagittal slices for DM and non-DM animals. The results of this analysis are shown in Figure 4. Five clusters ($K = 5$) were used for optimal visualization of the pattern differences between DM and non-DM animals (Figure 4(a) and (b)). The different clusters were associated with different anatomical areas, including tissue immediately associated with paravascular areas (zone 1, red and light blue), tissue immediately adjacent to zone 1 (zone 2, green), and the most distally labeled voxels next to zone 2 (zone 3, dark blue), respectively, and green and dark blue represent the intermediate (green) and slow (dark blue) parenchymal glymphatic pathways. The TECs of the five clusters from the DM **(C)** and non-DM **(D)** rats show that the most proximal paravascular conduits (red and

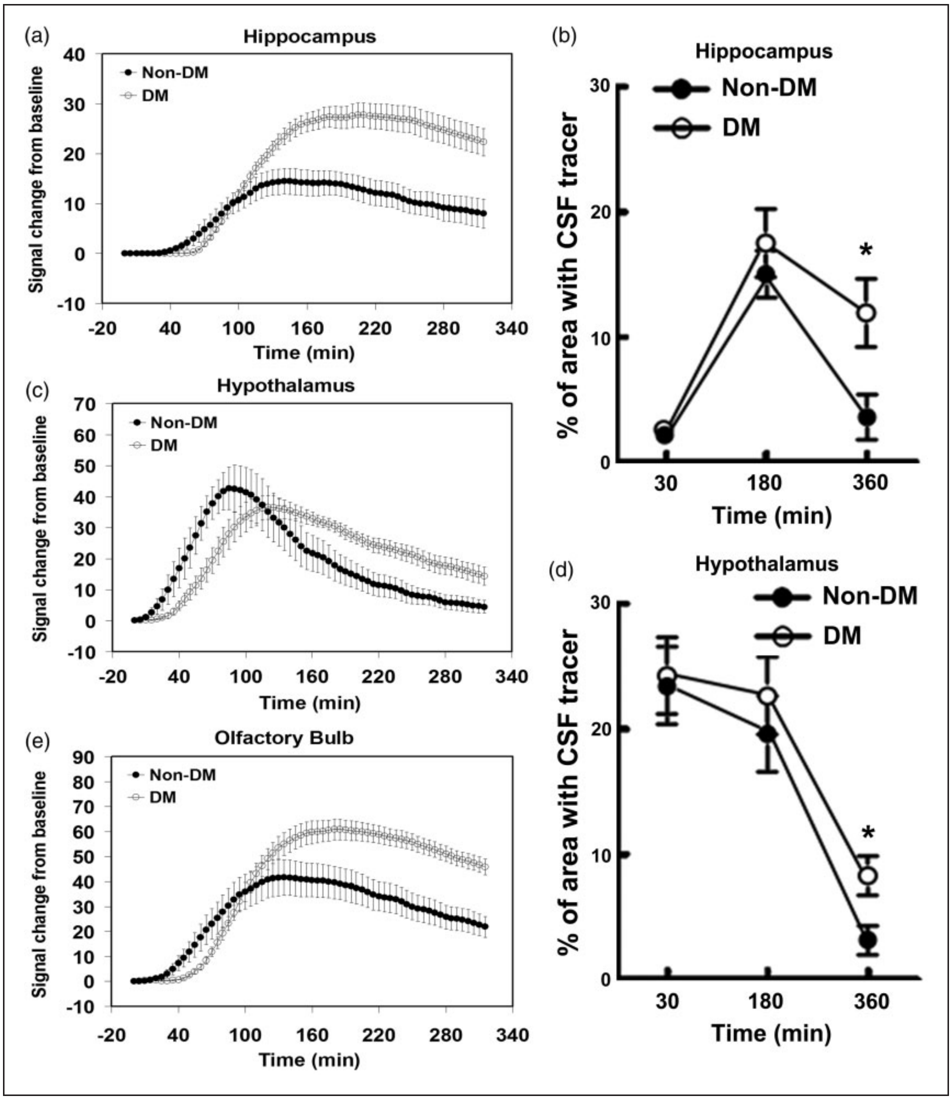

Figure 3. Quantitative time evolution differences in hippocampus, hypothalamus, and olfactory bulb between non-DM and DM groups: MRI time evolution curve in hippocampus (a), hypothalamus (c), and olfactory bulb (e) indicate that DM-induced higher residual tracer concentrations and slower clearance rate than non-DM group which was confirmed by fluorescence microscopic image results (b and d).

light blue clusters) are represented by the highest signal changes when compared with the green (intermediate) and blue (slow) clusters (Figure 4(c) and (d)). Although it initially appears as if there are no signal changes in the background cluster (black, cluster 5), dynamically increased signal intensity after Gd-DTPA injection is evident in the areas with cluster five, when the Y scale resolution in Figure 3(c) and (d) is increased. The DM animal exhibited larger paravascular areas ($p = 0.043$, zone 1, 440%), smaller mean value of zone two areas ($p = 0.201$, 84%), and similar zone three areas ($p = 0.597$, 105%) compared with non-DM animals. Also, the olfactory bulb region was dominant with zone 1 and 2 areas in the DM animal but with zone 2 and 3 areas in the non-DM animal (Figure 4(a) and (b)). The zone 2 areas in the DM animal were smaller with marginal significance ($p = 0.065$, 76%) than that in the non-DM animal, if the olfactory bulb region was excluded. Therefore, the cluster data suggest that DM significantly increases the paravascular space, and that the large accumulation of solutes in the DM animal may be caused by a reduced clearance of intermediate solute glymphatic pathway.

Impairment of CSF-ISF exchange is significantly correlated with cognitive deficits in the DM brain

The DM-induced structural and functional deficits in certain brain regions such as the hippocampus and cerebral cortex are associated with learning and

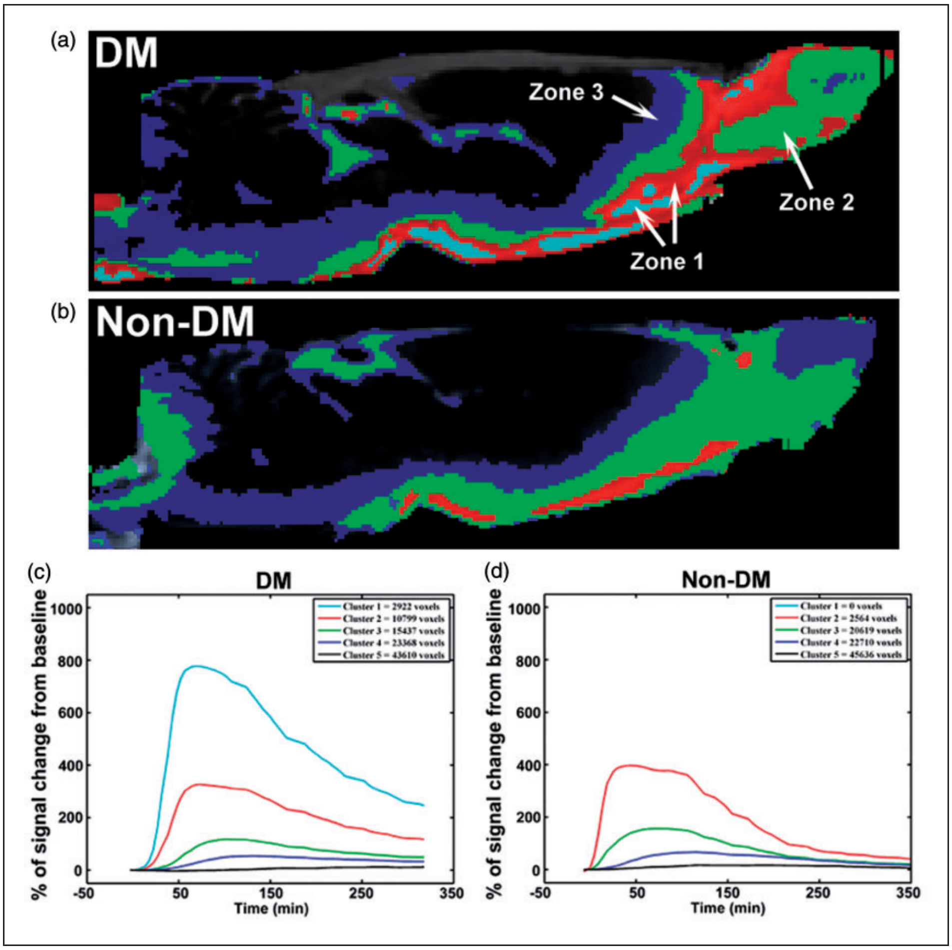

Figure 4. Cluster-based spatial distribution of Gd-DTPA between representative non-DM and DM rats: Cluster analysis of DM rat (a) exhibited larger paravascular cluster (light blue and red, zone 1) and smaller intermediate parenchymal glymphatic pathways (green, zone 2), especially in other brain areas except the olfactory bulb compared with non-DM (b) rat. Panels C and D display the TECs for each of the 5 clusters with the total number of voxels for DM (c) and non-DM (d) rats.

memory deficits.[31–33] Our observation on DM-induced impairment of the glymphatic system in the hippocampus prompted us to examine the relationships between cognitive deficits and impairments on ISF clearance. To examine cognitive function, spatial learning function and olfactory learning and memory were examined by means of MWM and odor recognition tests. Rats with DM spent significantly less time in the correct quadrant of MWM compared to non-DM rats (Figure 5(a)). In addition, DM rats also spent much less time on a novel object measured by the odor recognition test (Figure 5(b)). These data indicate that the impairment of learning and memory occurs after DM (Figure 5). A significant linear relationship between the accumulation of TR-d3 level in the hippocampus 6 h after ICM injection and the cognitive deficits measured by the MWM ($r^2 = 0.948$, Figure 5(c)) and odor recognition tests ($r^2 = 0.991$, Figure 5(d)) was detected in the DM and non-DM rat. We also examined the relationships between MRI parameters of glymphatic impairment and the cognitive deficits in both of hippocampus and hypothalamus. Stronger correlation with the cognitive deficits was detected for MRI residual intensity (MWM, $r^2 = 0.856$ and $r^2 = 0.855$; ODOR, $r^2 = 0.861$ and $r^2 = 0.882$ for hippocampus and hypothalamus, respectively) compared to MRI clearance rate constant (MWM, $r^2 = 0.493$ and $r^2 = 0.406$; ODOR, $r^2 = 0.485$ and $r^2 = 0.414$ for hippocampus and hypothalamus, respectively).

Discussion

DM is a major risk factor for cognitive dysfunction in the elderly. However, preclinical studies on the impact of DM during cognitive aging are limited. Using NTM and STZ, we induced hyperglycemia by provoking defective insulin secretion in pancreatic β-cells in the middle-aged rats, which resembles the clinical

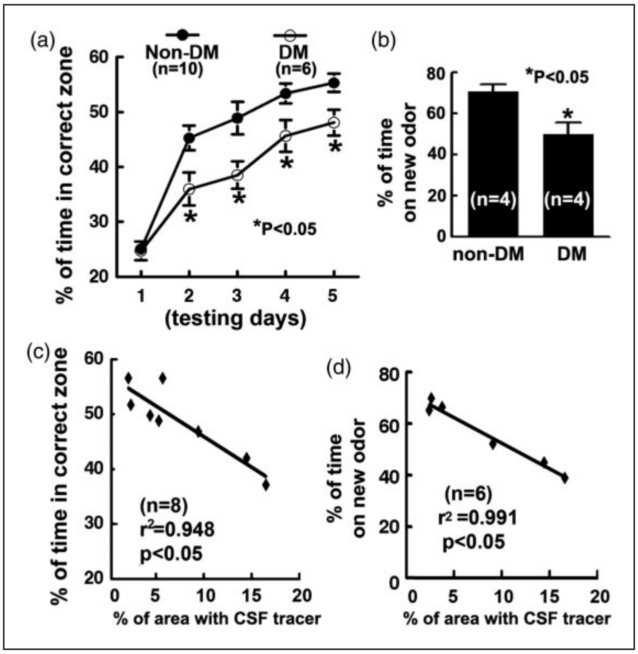

Figure 5. Functional deficits and correlations: Panels A and B show impairments of spatial learning spatial learning function and the olfactory learning and memory measured by the Morris water maze test (a) and odor recognition test (b) in rats after T2DM. Scatter plot graphs C and D show the correlation between the percentage areas with low molecular weight tracer TR-d3 measured 6 h after ICM injection and the water maze test scores (day 5, c), and odor recognition test scores (d) in DM and non-DM rats.

manifestation of T2DM.[24] More importantly, these rats develop profound cognitive deficits compared to the age-matched non-DM rat two months after induction of DM. Thus, we, for the first time, have established a DM model in the middle-aged rat that leads to the development of cognitive decline. Our model is directly relevant to the cognitive dysfunction observed in patients with DM. In attempting to identify the role of glymphatic system in DM-associated cognitive deficits, we performed the first investigation of glymphatic system impairment after DM. Our data demonstrate that DM induces impairment of the glymphatic system which is highly correlated with cognitive deficits. Quantitative MRI measurements provide sensitive markers for glymphatic impairment after DM.

Contradicting the traditional model of CSF hydrodynamics, recent studies demonstrated that a large proportion of subarachnoid CSF re-circulates through the brain parenchyma via paravascular spaces and exchanges with the ISF, and exits along para-venous pathways.[9–13] In parallel, the present study shows that following ICM administration, contrast agent moves rapidly by bulk flow through para-arterial pathways to reach major influx nodes at the pituitary recess, the olfactory bulb, and the pineal recess in both DM and non-DM animals. We also demonstrated, similar as previous study,[30] that MRI tracer efflux along the SS sinus (Figure 2). However, compared with age-matched non-DM rats, the T2DM rats increased residual intensity and decreased clearance rate constant by 7.72 and 3.41 times of non-DM rats in the hippocampus, respectively. Our results confirm and extend the original model of glymphatic fluxes.[9–13] Most importantly, our results provide the first insight into the pathophysiological impairment of glymphatic fluxes in DM. DM-induced slow clearance of solutes depends on region in brain parenchyma. Compared with non-DM animals, DM animals exhibited a larger decrease in clearance rate constant and increase in residual Gd-DTPA in the hippocampus. These large differences are most likely caused by both regionally specific slower clearance rate constants and DM-induced increased delay in the hippocampus. The MRI results also were confirmed by ex vivo measurements showing significant larger TR-d3 tracer areas in the hippocampus of DM rats compared with non-DM rats 6 h after TR-d3 injection. Therefore, the quantitative MRI measurements of impairment of the glymphatic system may provide sensitive markers in detecting diabetes-associated brain abnormalities and can be employed to clinic as demonstrated in recent publication.[34]

The prevalence of cognitive dysfunction and development of Alzheimer Disease (AD) is high in diabetic patients, especially among the elderly, suggesting that diabetes plays an important role in the development of cognitive impairment and AD.[35,36] Studies have demonstrated that hyperglycemia induces cerebral neurovascular dysfunction, oxidative stress, neurotoxicity, and defects in neural insulin and amyloid metabolism, all of which been implicated in the development of cognitive abnormalities.[37] However, the mechanisms underlying cognitive impairment associated with DM remain to be investigated. In the present study, DM-induced cognitive decline measured by MWM and odor recognition tests was highly correlated with MRI residual intensity in both hippocampus and hypothalamus which was confirmed by ex-vivo fluorescence imaging results. Our data provide correlative evidence linking DM-induced impairment of ISF clearance with cognitive deficits. However, we speculate that failure of glymphatic function is not necessary cause of the impairment of retrograde memory. An important neuropathological mechanism in the diabetic brain is the accumulation of misaggregated proteins, including senile plaques comprised of amyloid-β (Aβ),[38,39] which have been shown to affect cognitive function. Thus, an elevated residual of solutes in the hippocampus in the diabetic brain may increase the accumulation of Aβ and other molecules that may induce cognitive impairments. Indeed, previous studies have demonstrated that the glymphatic system regulates the clearance of Aβ.[11] Patients with T2DM who developed AD exhibited extensive accumulation of Aβ and neuritic plaques.[40] Experimental studies show that diabetes induced by high-fat and/or sugar diet (HFD) leads to Aβ accumulation in the brain.[41–45] In addition, it is likely that the impairment of the glymphatic system and associated accumulation of molecular waste in the paravascular space activate a cascade of inflammatory responses that lead to neurovascular disruption, including the increase of the paravascular space, a pathological feature in DM brain and other dementia diseases.[46] Thus, the cumulative Aβ deposition and neurovascular disruption following glymphatic impairment may facilitate a positive feed-back loop, further adversely affecting glymphatic system function in the DM brain. However, whether DM-induced impairment of glymphatic system function promotes Aβ-mediated neuropathology and neurovascular damage warrants further investigation.

Similar to the hippocampus with a different dynamic profile, the hypothalamus also exhibited significant increases of residual Gd-DTPA in DM animals. Hypothalamic nuclei have a well-established role in modulating energy homeostasis and feeding regulation, and alterations in neuroregulatory pathways in hypothalamus can lead to modifications of central and peripheral control in food intake and energy expenditure.[47,48] The impairment of the glymphatic system in the hypothalamus of the T2DM animal detected by MRI, therefore, may alter central and peripheral control in food intake and energy expenditure.

To directly visualize the changes of slow, intermediate, and fast parenchymal glymphatic pathways after DM, we also performed a cluster analysis for DM and non-DM animals adapting a previously published strategy.[14] Increased areas with fast glymphatic pathways and decreased areas with intermediate glymphatic pathways were detected in the diabetic brain. The explanation of the distinguished feature of the cluster results may indicate that the slow clearance of solutes after diabetes dominantly contributes from reduced capability of intermediate glymphatic pathways which in turn increased para-arterial areas with elevated solute concentration. Our data demonstrated that the CSF contrast influx from the paravascular space was comparable between T2DM and non-DM rats and the increased areas with fast glymphatic pathways (zone 1 in cluster analysis) may be induced by enlarged paravascular space. Diabetes induces both micro- and macro-vascular damage which increase the risk of developing small vessel disease with enlargement of the perivascular space.[15,16] Diabetes is a common feature in patients with cortical atherothromboembolism and lacunar stroke[49] which alter arteriolar structure and increase the perivascular space.[15,16,50] Inflammation may also play an important role in the enlargement of the perivascular space. Previous studies have suggested that active inflammation in multiple sclerosis and in lacunar stroke increases perivascular space.[46,51] Inflammatory cell infiltrates have been noted pathologically in penetrating arterioles and perivascular tissue in patients with small vessel disease.[52] Plasma inflammatory markers are increased in patients with lacunar stroke[51,53] associated genetically with progression of white matter hyperintensities and lacunar infarcts.[54] The enlarged paravascular space could also be one factor for reducing clearance of Gd-DTPA due to stagnation of glymphatic transport. The advantage of the MRI cluster analysis is its direct visualization and identification for the affected parts of the glymphatic system by disease. Potentially, cluster analysis of glymphatic pathways can also be employed to detect treatment effects in neurological diseases, include diabetes.

Our data demonstrated for the first time, that diabetes adversely affects glymphatic system function, which is highly associated with impairment of learning and memory. MRI can provide sensitive quantitative measurements of glymphatic impairment after DM and may potentially have clinical application due to its non-invasive nature. However, based on the present study, we cannot claim that failure of glymphatic function is the cause of the impairment of cognitive deficits. Further investigations are required to mechanistically relate the glymphatic dysfunction to cognitive impairment.

Funding

The author(s) disclosed receipt of the following financial support for the research, authorship, and/or publication of this article: This work was supported by NIH grants RO1 NS064134 (Jiang), R21AG052735 (Jiang), NS079612 (ZG Zhang), NS062832 (L Zhang), AG037506 (Chopp).

Declaration of conflicting interests

The author(s) declared no potential conflicts of interest with respect to the research, authorship, and/or publication of this article. The content is solely the responsibility of the authors and does not necessary represent the official view of the National Institute of Health.

Authors' contributions

Substantial contributions to conception and design: QJ, LZ and ZZ; Acquisition of data, or analysis and interpretation of data: GD, ED-B, QJ, LZ, LL, QL, NS; Drafting the article or revising it critically for important intellectual content: QJ, MC, LZ, MN and ZZ; Final approval of the version to be published: QJ, MC, LZ, MN and ZZ.

References

1. Janghorbani M, Hu FB, Willett WC, et al. Prospective study of type 1 and type 2 diabetes and risk of stroke subtypes: the Nurses' Health Study. *Diab Care* 2007; 30: 1730–1735.
2. Giorda CB, Avogaro A, Maggini M, et al. Incidence and risk factors for stroke in type 2 diabetic patients: the DAI study. *Stroke* 2007; 38: 1154–1160.
3. Peila R, Rodriguez BL, White LR, et al. Fasting insulin and incident dementia in an elderly population of Japanese-American men. *Neurology* 2004; 63: 228–233.
4. Qiu C, Cotch MF, Sigurdsson S, et al. Retinal and cerebral microvascular signs and diabetes: the age, gene/environment susceptibility-Reykjavik study. *Diabetes* 2008; 57: 1645–1650.
5. Luchsinger JA, Tang MX, Shea S, et al. Hyperinsulinemia and risk of Alzheimer disease. *Neurology* 2004; 63: 1187–1192.
6. Craft S and Watson GS. Insulin and neurodegenerative disease: shared and specific mechanisms. *Lancet Neurol* 2004; 3: 169–178.
7. Gispen WH and Biessels GJ. Cognition and synaptic plasticity in diabetes mellitus. *Trends Neurosci* 2000; 23: 542–549.
8. Luchsinger JA and Gustafson DR. Adiposity, type 2 diabetes, and Alzheimer's disease. *J Alzheimer Dis* 2009; 16: 693–704.
9. Xie L, Kang H, Xu Q, et al. Sleep drives metabolite clearance from the adult brain. *Science* 2013; 342: 373–377.
10. Iliff JJ, Wang M, Zeppenfeld DM, et al. Cerebral arterial pulsation drives paravascular CSF-interstitial fluid exchange in the murine brain. *J Neurosci* 2013; 33: 18190–18199.
11. Iliff JJ, Wang M, Liao Y, et al. A paravascular pathway facilitates CSF flow through the brain parenchyma and the clearance of interstitial solutes, including amyloid beta. *Sci Transl Med* 2012; 4: 147ra111.
12. Rangroo TV, Thrane AS, Plog BA, et al. Paravascular microcirculation facilitates rapid lipid transport and astrocyte signaling in the brain. *Sci Rep* 2013; 3: 2582.
13. Plog BA, Dashnaw ML, Hitomi E, et al. Biomarkers of traumatic injury are transported from brain to blood via the glymphatic system. *J Neurosci* 2015; 35: 518–526.
14. Iliff JJ, Lee H, Yu M, et al. Brain-wide pathway for waste clearance captured by contrast-enhanced MRI. *J Clin Invest* 2013; 123: 1299–1309.
15. Doubal FN, MacLullich AM, Ferguson KJ, et al. Enlarged perivascular spaces on MRI are a feature of cerebral small vessel disease. *Stroke* 2010; 41: 450–454.
16. Wardlaw JM, Smith C and Dichgans M. Mechanisms of sporadic cerebral small vessel disease: insights from neuroimaging. *Lancet Neurol* 2013; 12: 483–497.
17. McCrimmon RJ, Ryan CM and Frier BM. Diabetes and cognitive dysfunction. *Lancet* 2012; 379: 2291–2299.
18. Moheet A, Mangia S and Seaquist ER. Impact of diabetes on cognitive function and brain structure. *Ann N Y Acad Sci* 2015; 1353: 60–71.
19. Mayeda ER, Whitmer RA and Yaffe K. Diabetes and cognition. *Clin Geriat Med* 2015; 31: 101–115.
20. Masiello P, Broca C, Gross R, et al. Experimental NIDDM: development of a new model in adult rats administered streptozotocin and nicotinamide. *Diabetes* 1998; 47: 224–229.
21. Su HC, Hung LM and Chen JK. Resveratrol, a red wine antioxidant, possesses an insulin-like effect in streptozotocin-induced diabetic rats. *Am J Physiol Endocrinol Metabol* 2006; 290: E1339–E1346.
22. Kahn SE. The relative contributions of insulin resistance and beta-cell dysfunction to the pathophysiology of Type 2 diabetes. *Diabetologia* 2003; 46: 3–19.
23. Szkudelski T. Streptozotocin-nicotinamide-induced diabetes in the rat. Characteristics of the experimental model. *Exp Biol Med* 2012; 237: 481–490.
24. DeFronzo RA, Bonadonna RC and Ferrannini E. Pathogenesis of NIDDM. A balanced overview. *Diab Care* 1992; 15: 318–368.
25. Choi SH, Woodlee MT, Hong JJ, et al. A simple modification of the water maze test to enhance daily detection of spatial memory in rats and mice. *J Neurosci Meth* 2006; 156: 182–193.
26. Schallert T. Behavioral tests for preclinical intervention assessment. *NeuroRx* 2006; 3: 497–504.
27. Spinetta MJ, Woodlee MT, Feinberg LM, et al. Alcohol-induced retrograde memory impairment in rats: prevention by caffeine. *Psychopharmacology* 2008; 201: 361–371.
28. Fan X and Karczmar GS. A new approach to analysis of the impulse response function (IRF) in dynamic contrast-enhanced MRI (DCEMRI): a simulation study. *Magn Reson Med* 2009; 62: 229–239.
29. Iliff JJ, Chen MJ, Plog BA, et al. Impairment of glymphatic pathway function promotes tau pathology after traumatic brain injury. *J Neurosci* 2014; 34: 16180–16193.
30. Lee H, Xie L, Yu M, et al. The effect of body posture on brain glymphatic transport. *J Neurosci* 2015; 35: 11034–11044.
31. Biessels GJ, Kamal A, Ramakers GM, et al. Place learning and hippocampal synaptic plasticity in streptozotocin-induced diabetic rats. *Diabetes* 1996; 45: 1259–1266.
32. Baydas G, Nedzvetskii VS, Nerush PA, et al. Altered expression of NCAM in hippocampus and cortex may underlie memory and learning deficits in rats with streptozotocin-induced diabetes mellitus. *Life Sci* 2003; 73: 1907–1916.
33. Hasanein P and Shahidi S. Effects of combined treatment with vitamins C and E on passive avoidance learning and memory in diabetic rats. *Neurobiol Learn Memory* 2010; 93: 472–478.
34. Eide PK and Ringstad G. MRI with intrathecal MRI gadolinium contrast medium administration: a possible method to assess glymphatic function in human brain. *Acta Radiol Open* 2015; 4: 2058460115609635.
35. Baglietto-Vargas D, Shi J, Yaeger DM, et al. Diabetes and Alzheimer's disease crosstalk. *Neurosci Biobehav Rev* 2016; 64: 272–287.
36. Yaffe K, Blackwell T, Kanaya AM, et al. Diabetes, impaired fasting glucose, and development of cognitive impairment in older women. *Neurology* 2004; 63: 658–663.

37. Qiu C, Sigurdsson S, Zhang Q, et al. Diabetes, markers of brain pathology and cognitive function: the Age, Gene/Environment Susceptibility-Reykjavik Study. *Ann Neurol* 2014; 75: 138–146.
38. Prasad S, Sajja RK, Naik P, et al. Diabetes mellitus and blood-brain barrier dysfunction: an overview. *J Pharmacovigil* 2014; 2: 125.
39. Szeman B, Nagy G, Varga T, et al. [Changes in cognitive function in patients with diabetes mellitus]. *Orvosi Hetilap* 2012; 153: 323–329.
40. Janson J, Laedtke T, Parisi JE, et al. Increased risk of type 2 diabetes in Alzheimer disease. *Diabetes* 2004; 53: 474–481.
41. Ho L, Qin W, Pompl PN, et al. Diet-induced insulin resistance promotes amyloidosis in a transgenic mouse model of Alzheimer's disease. *FASEB J* 2004; 18: 902–904.
42. Yang Y, Wu Y, Zhang S, et al. High glucose promotes Abeta production by inhibiting APP degradation. *PloS One* 2013; 8: e69824.
43. Vandal M, White PJ, Tremblay C, et al. Insulin reverses the high-fat diet-induced increase in brain Abeta and improves memory in an animal model of Alzheimer disease. *Diabetes* 2014; 63: 4291–4301.
44. Mehla J, Chauhan BC and Chauhan NB. Experimental induction of type 2 diabetes in aging-accelerated mice triggered Alzheimer-like pathology and memory deficits. *J Alzheimer Dis* 2014; 39: 145–162.
45. Cao D, Lu H, Lewis TL, et al. Intake of sucrose-sweetened water induces insulin resistance and exacerbates memory deficits and amyloidosis in a transgenic mouse model of Alzheimer disease. *J Biol Chem* 2007; 282: 36275–36282.
46. Wuerfel J, Haertle M, Waiczies H, et al. Perivascular spaces – MRI marker of inflammatory activity in the brain? *Brain* 2008; 131(Pt 9): 2332–2340.
47. Morton GJ and Schwartz MW. Leptin and the central nervous system control of glucose metabolism. *Physiol Rev* 2011; 91: 389–411.
48. Abizaid A and Horvath TL. Brain circuits regulating energy homeostasis. *Regul Pept* 2008; 149: 3–10.
49. Jackson CA, Hutchison A, Dennis MS, et al. Differing risk factor profiles of ischemic stroke subtypes: evidence for a distinct lacunar arteriopathy? *Stroke* 2010; 41: 624–629.
50. Giwa MO, Williams J, Elderfield K, et al. Neuropathologic evidence of endothelial changes in cerebral small vessel disease. *Neurology* 2012; 78: 167–174.
51. Rouhl RP, Damoiseaux JG, Lodder J, et al. Vascular inflammation in cerebral small vessel disease. *Neurobiol Aging* 2012; 33: 1800–1806.
52. Bailey EL, Smith C, Sudlow CL, et al. Pathology of lacunar ischemic stroke in humans – a systematic review. *Brain Pathol* 2012; 22: 583–591.
53. Hassan A, Hunt BJ, O'Sullivan M, et al. Markers of endothelial dysfunction in lacunar infarction and ischaemic leukoaraiosis. *Brain* 2003; 126(Pt 2): 424–432.
54. Fornage M, Chiang YA, O'Meara ES, et al. Biomarkers of inflammation and mri-defined small vessel disease of the brain: the cardiovascular health study. *Stroke* 2008; 39: 1952–1959.